Article:
Chen, W, Kemp, DB, He, T orcid.org/0000-0001-8975-8667 et al. (7 more authors) (2023) Shallow- and deep-ocean Fe cycling and redox evolution across the Pliensbachian–Toarcian boundary and Toarcian Oceanic Anoxic Event in Panthalassa. Earth and Planetary Science Letters, 602. 117959. ISSN 0012-821X

https://doi.org/10.1016/j.epsl.2022.117959

Shallow- and deep-ocean Fe cycling and redox evolution across the Pliensbachian–Toarcian boundary and Toarcian Oceanic Anoxic Event in Panthalassa

Wenhan Chen[1], David B. Kemp[1*], Tianchen He[2], Robert J. Newton[2], Yijun Xiong[2], Hugh C. Jenkyns[3], Kentaro Izumi[4], Tenichi Cho[5], Chunju Huang[1], Simon W. Poulton[2,6]

[1]*State Key Laboratory for Biogeology and Environmental Geology and Hubei Key Laboratory of Critical Zone Evolution, School of Earth Sciences, China University of Geosciences (Wuhan), Wuhan 430074, P.R. China*

[2]*School of Earth and Environment, University of Leeds, Leeds LS2 9JT, UK*

[3]*Department of Earth Sciences, University of Oxford, South Parks Road, Oxford OX1 3AN, UK*

[4]*Faculty and Graduate School of Education, Chiba University, 1-33 Yayoi-cho, Inage-ku, Chiba-shi, Chiba 263-8522, Japan*

[5]*Graduate School of Creative Science and Engineering, Waseda University, Tokyo 169-8050, Japan*

[6]*State Key Laboratory of Geological Processes and Mineral Resources, China University of Geosciences (Wuhan), Wuhan 430074, P.R. China*

*Corresponding author: David B. Kemp (davidkemp@cug.edu.cn)

Abstract

The late Pliensbachian to early Toarcian was characterized by major climatic and environmental changes, encompassing the early Toarcian Oceanic Anoxic Event (T-OAE, or Jenkyns Event, ~183 Ma) and the preceding Pliensbachian–Toarcian boundary event (Pl/To). Information on seawater redox conditions through this time interval has thus far come mainly from European sections deposited in hydrographically restricted basins, and hence our understanding of the redox evolution of the open ocean (and in particular Panthalassa – the largest ocean to have existed) is limited. Here, we present high-resolution Fe-speciation and redox-sensitive trace metal data from two Panthalassic Ocean sections across the Pl/To and the T-OAE intervals, one deposited in deep water (paleo-water depth >~2.7 km) and the other on a shallow margin (paleo-water depth likely <~50 m). Data from the deep-water open-ocean site indicate anoxic-ferruginous conditions from the late Pliensbachian to the end of the T-OAE, with potentially more intense development of sulfidic pore waters at the sediment-water interface around the Pl/To boundary. At least intermittent bottom-water euxinia characterized the T-OAE, followed by a subsequent transition toward more oxygenated conditions. By contrast, trace metal data from the shallow margin site indicate that oxygenated to possibly suboxic conditions prevailed. However, elevated highly reactive iron contents, dominated by Fe (oxyhydr)oxides, characterize this shallow-water site. These observations suggest that upwelling, driven in part by increased sea level and prevailing winds from the open ocean, brought anoxic-ferruginous waters onto the shelf, whereupon Fe^{2+} oxidation was initiated in oxic shallow waters.

1. Introduction

The early Toarcian Oceanic Anoxic Event (T-OAE; ~183 Ma) was one of the most significant environmental perturbations of the Phanerozoic, and was associated with widespread deposition of organic carbon-rich sediments in low-oxygen environments (Jenkyns, 1988), a minor mass extinction (Little and Benton, 1995), and a pronounced negative carbon-isotope excursion (CIE) linked to a substantial injection of ^{12}C-enriched carbon into the biosphere, termed the Jenkyns Event (Hesselbo et al., 2000; Erba et al., 2022). A smaller magnitude carbon-cycle perturbation occurred at the preceding Pliensbachian–Toarcian boundary (Pl/To), and this has been similarly linked to carbon release (e.g., Littler et al., 2010). Sulfur- and Mo-isotope data support a global expansion of anoxic seawater conditions across the T-OAE (Gill et al., 2011; Newton et al., 2011; Dickson, et al., 2017), while Tl-isotope data suggest globally protracted reducing conditions that initiated at the Pl/To (Them et al., 2018). Nevertheless, the extent and significance of deoxygenation in individual sites and basins was geographically variable during the T-OAE (e.g., Remírez and Algeo, 2020; Chen et al., 2021; Kemp et al., 2022a), and a paucity of marine redox analyses across the Pl/To means that the redox response across this event is unclear.

Information on open-ocean redox changes across the Pl/To and T-OAE intervals, and the effects of these events on the global Fe cycle, is limited owing to a lack of deep-water sections best suited to reveal changes in Fe cycling representative of the pelagic realm. Here, we report Fe-speciation data and redox-sensitive trace element concentrations from two Panthalassic Ocean records across the Pl/To and T-OAE intervals; one deposited in the deep ocean and the other on a shallow-water continental margin. These data provide a unique window into the redox evolution of the extensive Panthalassa from the late Pliensbachian to the early Toarcian, allowing us to place new constraints on the behavior of the Fe cycle during these two ancient episodes of potentially significant widespread anoxia.

2. Geological setting and age control

2.1 Sakuraguchi-dani section, Toyora area

Lower Jurassic shallow marine siliciclastic sedimentary rocks of the Toyora Group are exposed in the northern part of the Tabe Basin in the Toyora area of Yamaguchi Prefecture, SW Japan (Fig. 1). These strata were deposited on an active continental margin, paleogeographically close to the northern extremity of the South China Craton (northwestern margin of Panthalassa), based on provenance analysis of detrital zircon U-Pb data (Izumi et al., 2020). The Sakuraguchi-dani section is well exposed in streambeds close to Toyota Town (34°08′N 131°03′E; Fig. 1C). The Nishinakayama Formation at this section consists primarily of silty mudstones and fine-grained sandstones deposited above storm wave base (i.e., likely <50 m water depth). An ~3.5‰ negative excursion in organic-carbon isotopes ($\delta^{13}C_{org}$) occurs across an ~35 m thick interval of the Nishinakayama Formation (Izumi et al., 2012; Kemp and Izumi, 2014; Izumi et al., 2018a; Fig. 2A). This excursion can be unambiguously correlated with similar excursions in Europe and elsewhere, which characterize the T-OAE (see Fig. 5 in Izumi et al., 2018a). Additionally, detailed ammonite biostratigraphy of this section also supports an early Toarcian age coeval with the T-OAE in Europe (Izumi et al., 2012; Kemp and Izumi, 2014 and references therein). A CIE associated with the Pl/To boundary is not recognized, most likely due to a lack of outcrop.

2.2 Sakahogi section, Inuyama area

Deep-sea thinly bedded radiolarian cherts of Early Triassic to Early Jurassic age, and hemipelagic siliceous mudstones of Middle Jurassic age, occur north of Inuyama city along the banks of the Kiso River in Gifu Prefecture, central Japan (Fig. 1), and are repeated as thrust sheets named CH-1, CH-2, CH-3, and CH-4 in structurally ascending order (Fig. 1D). The Katsuyama and Sakahogi sections are located in CH-2 and CH-3, respectively (Fig. 1D). Paleomagnetic data suggest a low-latitude depositional location during the Jurassic, close to the equatorial divergence zone and thousands of kilometers from the Pangean landmass (Ando et al., 2001). The studied Sakahogi section near Inuyama (35°25'N 136°58'E) was deposited in the deep Panthalassa below the calcite compensation depth (CCD), and is preserved as part of a subduction-accretion complex (Matsuda and Isozaki, 1991). Deposition in Panthalassa below the CCD implies a minimum paleodepth of ~2.7 km for the cherts, assuming that the sediments do not derive from a seamount (e.g., Gröcke et al., 2011). At the Sakahogi section, green-grey bedded carbonate-free radiolarian cherts are interrupted by two distinctive black chert intervals, both associated with CIEs that are interpreted to represent the Pl/To and T-OAE, respectively (Ikeda et al., 2018; Kemp et al., 2022b; Fig. 2B). These age interpretations are constrained by radiolarian biostratigraphy and cyclostratigraphy (e.g., Ikeda and Hori, 2014; Ikeda et al., 2018 and references therein).

3. Materials and Methods

3.1 Samples

At the Sakuraguchi-dani section, 77 samples were analyzed for Fe-speciation and bulk elemental concentrations through the ~70 m sectionn encompassing the T-OAE CIE interval. Average sampling resolution was ~0.9 m though the entire succession, with higher resolution (~0.7 m) sampling within the CIE interval. At the Sakahogi section, 43 samples spanning the Pl/To CIE and the T-OAE CIE intervals (across an ~250 cm interval) were analyzed for Fe-speciation, with an average sampling resolution of ~6 cm. Elemental concentration data for the Sakahogi samples are from Kemp et al. (2022b).

3.2 Iron-speciation analysis

Fe-speciation has been widely used to identify water-column redox conditions in modern and ancient marine settings (e.g., Lyons and Severmann, 2006; Poulton and Canfield, 2011). Redox states are determined by evaluating the abundance of the highly reactive iron (Fe_{HR}) fraction relative to the total iron (Fe_T) pool. Highly reactive iron refers to the iron minerals that react with aqueous sulfide to form pyrite on diagenetic timescales (Canfield et al., 1992; Poulton et al., 2004), and comprises operationally defined Fe pools that target carbonate-associated Fe (Fe_{CARB}; including siderite and ankerite), ferric (oxyhydr)oxides (Fe_{OX}; including ferrihydrite, lepidocrocite, goethite and hematite), mixed ferrous–ferric minerals (Fe_{MAG}; dominantly magnetite), and Fe sulfides (Fe_{PY}; including iron monosulfides and pyrite) (Poulton and Canfield, 2005). Fe_{HR}/Fe_T ratios $\leq$0.22 generally indicate oxic bottom-water conditions, whereas Fe_{HR}/Fe_T $\geq$0.38 generally reflect anoxic conditions (Raiswell and Canfield, 1998; Poulton and Raiswell, 2002). In addition, the extent of pyritization of highly reactive Fe (Fe_{PY}/Fe_{HR}) can discern whether the bottom water was ferruginous (anoxic waters containing aqueous Fe^{2+}; Fe_{PY}/Fe_{HR} <0.6) or euxinic (anoxic and containing free H_2S; Fe_{PY}/Fe_{HR} >0.6–0.8) (Poulton, 2021).

Iron speciation analyses were conducted via standard techniques (Poulton and Canfield, 2005) in the Cohen Geochemistry Laboratory, University of Leeds and the State Key Laboratory of Biogeology and Environmental Geology, China University of Geosciences (Wuhan). In detail, ~0.1 g of sample powder was reacted with a 10 mL solution of 1M sodium acetate and acetic acid at 50°C for 48 h to extract iron in carbonates. Subsequently, the residue was mixed with a 10 mL solution of sodium dithionite and sodium citrate for 2 h to dissolve Fe (oxyhydr)oxides. The Fe_{MAG} pool was then extracted through the addition of a 10 mL solution of ammonium oxalate for 6 h. Fe_{PY} was determined by the chromium reduction method on separate splits of each sample (Canfield et al., 1986). Here, the sample powder (1–2 g) was treated with ~40 mL of 1 M reduced chromium chloride ($CrCl_2$) solution and 20 mL of 6 M HCl for 1 h, and the produced hydrogen sulfide (H_2S) was purged under a nitrogen atmosphere before being trapped as Ag_2S by bubbling through an $AgNO_3$ solution (0.1 M). The amount of sulfide in the sample was then determined by gravimetry after filtration and drying of the Ag_2S. The amount of pyrite iron hosted in the original sample was then calculated stoichiometrically. The iron concentration of each sequential extract was obtained using a ThermoFisher iCE 3300 atomic absorption spectrometer (AAS). Replicate extractions of samples and reference material WHIT (a Lower Jurassic fine-grained, laminated, organic carbon-rich mudstone deposited in an anoxic water column; see Alcott et al., 2020 for details) yielded relative standard deviations (RSDs) of <5% for all highly reactive Fe phases at both the University of Leeds and the China University of Geosciences (Wuhan). Silicate-hosted iron (Fe_{sil}) reflective of detrital iron influx was determined as the difference between total iron and highly reactive iron.

3.3 Bulk elemental concentrations

Approximately 80 mg of each powdered sample was dissolved in a HNO_3–HF–$HClO_4$ mixture, followed by evaporation to dryness. Boric acid was then added to the residue and heated to dryness, and the samples were then re-dissolved in hot HNO_3. Major (Al, Ca, Na, and K) and trace elements (Mo and U) were measured using a ThermoFisher iCAP 7400 radial inductively coupled plasma optical emission spectrometer (ICP-OES) and a ThermoFisher iCAP Qc inductively coupled plasma mass spectrometer (ICP-MS), respectively, in the Cohen Geochemistry Laboratory, University of Leeds. Total Fe concentrations (Fe_T) were measured using a ThermoFisher iCE 3300 atomic absorption spectrometer (AAS). Accuracy was monitored by analyzing the certified reference material USGS Eocene Green River Shale (SGR-1). Multiple replicate analyses of samples yielded RSDs for all elements of better than 3%.

To provide further insight, we utilized enrichment factors (EFs) to evaluate the abundance of redox-sensitive trace elements (RSTEs) Mo and U, quantified as $X_{EF} = (X/Al)_{sample}/(X/Al)_{UCC}$, where UCC refers to average upper continental crust composition (from McLennan, 2001; Fig. 3)

The CIA (chemical index of alteration) parameter has been widely used to reflect changes in continental chemical weathering (see Nesbitt and Young, 1982), and is calculated based on the formula: CIA=$[Al_2O_3/(Al_2O_3+CaO^*+Na_2O+K_2O)] \times 100$. The molecular proportions of the metal oxides used here to calculate CIA are converted from the respective metal element concentrations. The correction to CaO* was made by assuming reasonable Ca/Na ratios in silicate material following methods in McLennan (1993).

4. Results

At the Sakuraguchi-dani section, Fe_{HR}/Fe_T ratios are broadly stable (median 0.45) and generally >0.38 through the succession (69 out of 77 samples), notwithstanding two outlying values (~1.0 at 12.41 m and ~0.1 at 28.90 m) within the T-OAE CIE interval (Fig. 3A). Fe_{PY}/Fe_{HR} ratios are mostly <0.6, ranging from approximately 0 to 0.74 (median 0.13), with generally relatively higher values through the lower part of the T-OAE CIE interval (-4.28–3.15 m, Fig. 3A). Fe_{PY}/Fe_{HR} values are >0.6 at three levels, two of which (0.67 at -2.38 m; 0.73 at 19.90 m) are within the CIE interval, and one (0.74 at 39.4 m) which occurs above the CIE interval (Fig. 3A). An increased Fe_{sil} fraction (up to ~3.5 wt%) is observed from the onset of the CIE interval to ~5 m. Subsequently, Fe_{sil} fraction decreases to ~1.7 wt% at ~11 m and remains relatively stable up-section (Fig. 3A). Fe_{OX} dominates the unsulfidized Fe_{HR} phases. The proportion of Fe_{PY} varies considerably through the succession. Relatively high Fe_{PY} is observed at three levels, with two of them (~-4–3 m and ~14–23 m) in the CIE interval, and one (39.4 m) above the CIE interval. The proportions of Fe_{CARB} and Fe_{MAG} remain largely stable through the succession (Fig. 3A).

U_{EF} values are low and relatively stable, ranging from 0.3 to 1.1 (median 0.4) throughout the succession (Fig. 3A). Mo_{EF} values are also low, but are more variable than U_{EF} values, ranging from 0.2 to 1.2 (median 0.7). There is a slight increase in Mo_{EF} from the onset of the CIE interval (~-5 m) to ~10 m, over which Mo_{EF} increases to a maximum of 1.2. Subsequently, Mo_{EF} gradually decreases and remains relatively stable (~0.5) up-section (Fig. 3A). CIA values (median 71) range from 61.1 to 76.2 for the Sakuraguchi-dani sediments, with an increase (up to 76) from the onset of the CIE interval, followed by a drop to ~70 up-section with fluctuations (Fig. S1).

At the Sakahogi section, Fe_{HR}/Fe_T values are considerably higher than 0.38 throughout most of the succession, ranging from approximately 0.5 to 1 (median 0.87), with a decreasing trend above the T-OAE CIE interval (i.e., above ~240 cm; Fig. 3B). Fe_{PY}/Fe_{HR} ratios are <0.6 throughout much of the succession, ranging from approximately 0 to 0.82 (median 0.14), but are higher and commonly exceed 0.6 in the T-OAE CIE interval. There is also an increase up to ~0.6 well below the Pl/To CIE interval, with values decreasing to <0.2 across the stage boundary (Fig. 3B). The Fe_{sil} fraction is generally low (median 0.3 wt%) through the succession, albeit with some high-value (>0.9 wt%) levels (e.g., 37–39 cm, 99–100 cm, 174.5–175 cm, 224 cm, and 248–278 cm; Fig. 3B). The samples are generally significantly enriched in ferrous-Fe phases, particularly Fe_{CARB} and Fe_{PY}, up to the end of the T-OAE CIE interval (234.5 cm). However, there are intervals where Fe_{OX} commonly dominates, particularly in the upper part of the Pl/To CIE interval (~100 cm) and in the sediments between the Pl/To and the T-OAE CIE intervals, as well as above the T-OAE CIE interval (Fig. 3B).

U_{EF} values range from 0.8 to 38.6 (median 8.8) through the succession. Values increase markedly from the upper Pliensbachian to the base of the Toarcian and stay at a high level (i.e., well in excess of average UCC) upwards, before decreasing abruptly above the T-OAE CIE interval. Mo_{EF} values range from 0.2 to 623.1 (median 48.4) through the succession and show a similar general trend to U_{EF} values (Fig. 3B).

5. Discussion

5.1 Marine redox conditions in the deep Panthalassa from the late Pliensbachian to the early Toarcian

At the Sakahogi section, high Fe_{HR}/Fe_{T} and low Fe_{PY}/Fe_{HR} ratios through the succession indicate largely ferruginous bottom water at least in the Panthalassic deep ocean around the paleo-equator from the late Pliensbachian until the onset of the T-OAE CIE interval (Fig. 3B). Such strong and prolonged deep-water reducing conditions within the equatorial divergence zone could have been attributable at least in part to high productivity associated with wind-driven divergence of surface waters and consequent upwelling of bio-limiting elements to surface waters (e.g., Gröcke et al., 2011). This effect would have enhanced primary productivity, and the subsequent rain of excess organic carbon would then have accelerated the consumption of seawater dissolved oxygen, leading to an expanded oxygen minimum zone. Previous work on redox- and productivity-sensitive element proxies at the Sakahogi section has also emphasized the likely importance of anoxia for promoting the preservation of organic matter at this location (Kemp et al., 2022b).

The slight increase in Fe_{PY}/Fe_{HR} to ~0.6 well below the Pl/To boundary may potentially indicate sporadic water-column euxinia, but could also reflect an interval of more extensive diagenetic pyrite formation (see below). The pronounced rise in Fe_{PY}/Fe_{HR} ratios (to values >0.8) coincident with continually elevated Fe_{HR}/Fe_{T} ratios across the T-OAE CIE interval suggests the development of at least intermittent euxinia in the water column, which terminated at the end of the T-OAE CIE interval, when

Fe_{PY}/Fe_{HR} ratios returned to low levels (Fig. 3B). The close coincidence between increased TOC and pyrite content across the T-OAE CIE interval at the Sakahogi section (Fig. 3B) suggests the redox change from anoxic-ferruginous to euxinic deep-water conditions was likely linked to enhanced organic matter loading. Increased organic matter supply to the seafloor during the T-OAE CIE interval could have significantly accelerated microbial sulfate reduction and yielded more sulfide in deep waters (Fig. 2B; Chen et al., 2022). A generally low Fe_{sil} fraction through the Sakahogi succession suggests a negligible associated detrital flux of Fe (oxyhydr)oxide minerals to the deep-water sediment, thus providing favorable conditions for the potential development of water-column euxinia (Fig. 3B; Poulton and Canfield, 2011).

Independent evidence from trace metals (i.e., U and Mo) provides additional support for anoxia and potential euxinia during the T-OAE (see also Kemp et al., 2022b). Uranium enrichments are common beneath anoxic bottom waters, regardless of whether euxinic or ferruginous conditions dominate (Anderson et al., 1989). By contrast, when a critical threshold of free H_2S is met under euxinic conditions, formation of particle-reactive thiomolybdates (Helz et al., 1996) can result in significant Mo enrichment in the sediment (Helz et al., 1996; Erickson and Helz, 2000).

U_{EF} values are high until the end of the T-OAE CIE interval (Fig. 3B), supporting persistent anoxia. Very low sedimentation rates at the Sakahogi section (e.g., Ikeda et al., 2018) could have partly aided enrichment of Mo and U (Liu and Algeo, 2020) and, in particular, this may be an explanation for relatively high Mo_{EF} values in non-euxinic parts of the deep Panthalassic Ocean section. However, a combination of high Mo_{EF} and commonly high Fe_{PY}/Fe_{HR} ratios (Fig. 3B) supports the presence of at least intermittent euxinia during the T-OAE CIE interval, in line with Mo_{EF}-U_{EF} co-variations (Fig. 4A; see also Kemp et al., 2022b). Black chert deposition and TOC enrichments of up to ~34 wt% (Fig. 3B) accompany these elevated Mo and U enrichments (Kemp et al., 2022b), with high TOC being consistent with more reducing conditions.

Additionally, an increase in pyrite sulfur concentrations (S_{PY}) and a positive shift in pyrite sulfur isotopes ($\delta^{34}S_{pyrite}$) across the T-OAE CIE interval has been interpreted as a consequence of enhanced pyrite burial associated with an expanded extent of anoxia/euxinia (Fig. 2B; Chen et al., 2022), although increased regional TOC loading may have also impacted the $\delta^{34}S_{pyrite}$ values through accelerating microbial sulfate reduction (Chen et al., 2022). Nevertheless, these combined observations support development of at least intermittent euxinia in the deep Panthalassa during the T-OAE CIE interval. Further independent evidence for anoxia and possible euxinia in the present-day Inuyama area during the early Toarcian derives from the occurrence of the gray-black pyrite-bearing cherts and the predominance of micron-scale (4.5–6.3 µm) framboidal pyrite at the nearby Katsuyama section (Wignall et al., 2010; Fig. 1D), as well as from redox-sensitive trace element data from the Katsuyama section through the Pl/To black chert interval (Fujisaki et al., 2016).

By contrast, intervals of higher Fe_{PY}/Fe_{HR} below the Pl/To CIE interval do not coincide with elevated Mo_{EF} values (Fig. 3B), and S_{PY} concentrations are also low (Fig. 2B). This evidence supports enhanced diagenetic pyrite formation, rather than euxinic water-column conditions. Similarly, elevated Mo_{EF} values in a limited number of samples across the Pl/To CIE interval do not coincide with elevated Fe_{PY}/Fe_{HR} (Fig. 3B), while S_{PY} values are also low (Fig. 2B). However, a decrease in reduced non-sulfidized iron phases (i.e., Fe_{CARB}) also occurs across the Pl/To boundary, concurrent with an increase in the Fe_{OX} fraction (Fig. 3B). These combined signals are complex and suggest redox fluctuations, with transitions between oxic and sulfidic conditions at the sediment-water interface and/or sulfidic bottom-waters. In this scenario, periodic oxygen diffusion into the sediment facilitated pyrite and Fe_{CARB} oxidation near the sediment-water interface, consistent with a large decrease in TOC (sandwiched by two high TOC levels) at a depth of 101.5 to 104.5, which occurs coincident with a particularly low pyrite concentration (Figs. 2 and 3). The Mo and U drawn down during anoxic/sulfidic intervals would be retained in this interval via re-adsorption to Fe oxides.

Subsequently, a large increase in TOC above 104.5 cm occurs coincident with increases in MoEF values and a slight increase in pyrite, suggesting a return to more sulfidic conditions. This is followed by another decline in TOC and pyrite up to the end of the Pl/To boundary interval, concurrent with increased Fe_{OX}, again suggesting oxygenation. In addition, the likely oxidation of organic matter within the Sakahogi sediment would lower pore-water pH, therefore lowering the saturation state of the carbonate-hosted iron phase and inhibiting Fe_{CARB} precipitation. Collectively, a fluctuating redox state, alternating between short-lived oxic and more sulfidic conditions likely occurred across the Pl/To boundary (Fig. 3B), and intervals of enhanced sulfide generation likely drove the relative increase in $\delta^{34}S_{pyrite}$ across the Pl/To boundary (Fig. 2B; Chen et al., 2022).

Above the T-OAE CIE interval, there is a progressive drop in both Fe_{HR}/Fe_{T} (to values that begin to approach the oxic-anoxic threshold value of 0.38) and Fe_{PY}/Fe_{HR} ratios (Fig. 3B), consistent with abrupt coeval decreases in Mo_{EF} and U_{EF}. This pattern suggests gradual contraction of water-column anoxia/euxinia and the onset of more oxygenated conditions in the Panthalassic deep water. This interpretation is also supported by multi-site Mo-isotope analyses, which indicate a contraction in the worldwide extent of seafloor euxinia after the T-OAE (Dickson et al., 2017). Taken together, the deep-water Panthalassa was dominated by, at least locally/regionally, anoxic-ferruginous conditions from the late Pliensbachian to the onset of the T-OAE CIE interval. Enhanced sub-seafloor sulfidic conditions (intercalated with possible short-lived oxic episodes) occurred around the Pl/To boundary. This redox state was followed by the development of intermittent water-column euxinia during the T-OAE CIE interval, and more oxygenated conditions thereafter.

5.2 Marine redox conditions on the shallow Panthalassa shelf in the early Toarcian

At the Sakuraguchi-dani section, Fe_{HR}/Fe_{T} values are high (generally in excess of the anoxic threshold of 0.38) through the succession, despite a likely dilution effect on Fe_{HR} enrichment due to higher sedimentation rates in the more proximal shelf environment (e.g., Lyons and Severmann, 2006). Ostensibly, these Fe_{HR}/Fe_{T} data indicate continuous anoxic-ferruginous conditions on the shallow Panthalassa shelf during the T-OAE CIE interval (Fig. 3A). However, generally low Mo_{EF} and U_{EF} values (Fig. 3A), combined with Mo_{EF}-U_{EF} co-variation (Fig. 4B), suggest that oxic–suboxic conditions were predominant at the Sakuraguchi-dani section.

The relatively shallow water depth (likely <50 m) at the Sakuraguchi-dani section, coupled with evidence for turbulent-water conditions (Izumi et al., 2018a), would likely have prevented development of a stable chemocline, thus helping to maintain oxygenated conditions or highly dynamic/fluctuating states between oxic and suboxic conditions during the T-OAE CIE interval. This supposition is also supported by previously published sedimentological data that indicate the common occurrence of unlaminated and bioturbated strata in the succession, particularly over the T-OAE CIE interval (Izumi et al., 2018a). In addition, previously published elemental data showed negligible enrichment of Mo, V and Cr at the Sakuraguchi-dani section, suggestive of largely oxic–suboxic conditions (Kemp and Izumi, 2014). Moreover, marked fluctuations in ichnofabric index data during the T-OAE CIE interval (Fig. 2A) also argue for a lack of sustained anoxia and frequent re-oxygenation, as illustrated by moderate to strong bioturbation (ichnofabric index ≥3) (Izumi et al., 2012; Kemp and Izumi, 2014).

A slight increase in Mo_{EF} values, combined with generally higher Fe_{PY}/Fe_{HR} ratios, through the lower part of the T-OAE CIE interval (Fig. 3A) potentially indicates deoxygenation with enhanced sulfide production, which may have included transient intervals of bottom-water euxinia. This suggestion is consistent with sparse framboidal pyrite and ichnofabric data (Izumi et al., 2012, 2018b). Such conditions could have led to the slight upward trend in S_{PY} observed at the onset of the T-OAE CIE interval, although the positive shift in $\delta^{34}S_{pyrite}$ between approximately -0.5 and 8 m in the CIE interval is likely primarily attributable to high sedimentation rates (Fig. 2A; Chen et al., 2022). High sedimentation rates reduce the connectivity of sedimentary pore waters to the overlying waters, limiting the resupply of seawater for microbial sulfate reduction through diffusion (Chen et al., 2022). These data notwithstanding, the clear disconnect between the Fe-speciation data (indicating persistent anoxia) and elemental, sedimentological and paleoecological information (indicating largely oxic–suboxic conditions) at the Sakuraguchi-dani section requires further analysis on the controls governing the marine Fe cycle.

5.3 Source and enrichment mechanism of highly reactive iron on the Panthalassa shelf

Previous studies have demonstrated a global enhancement of chemical weathering and hydrological cycling during the T-OAE CIE interval (e.g., Izumi et al., 2018a; Kemp et al., 2020). At the Sakuraguchi-dani section, increased advective sediment transport and the delivery of terrestrial plant detritus during the Toarcian CIE interval, coupled with evidence for sediment coarsening and the occurrence of possible hyperpycnites (Fig. 2A), represent a regional signature of this warming-induced enhancement of the hydrological cycle (Izumi et al., 2018a; Kemp et al., 2019). Enhanced chemical weathering increases the proportion of Fe_{HR} in terrestrial sediments, although in general Fe_{HR} enrichments are not transferred to the marine realm because of extensive preferential trapping in inner-shore regions (Poulton and Raiswell, 2002). However, recent analysis of Fe-cycle behavior has indicated a possible chemical weathering control on Fe_{HR} enrichments in marine sediments adjacent to mountainous regions that discharge sediment directly onto the continental shelf (Wei et al., 2021).

At the Sakuraguchi-dani section, the Fe_{sil} fraction is generally ~2 wt%, with an increase at the onset of the T-OAE CIE interval, diagnostic of an enhanced detrital iron influx (Fig. 3A). However, a negligible correlation (R^2 = 0.08, p = 0.04) is observed between the relative proportions of Fe_{sil} and Fe_{HR} across the T-OAE CIE interval (Fig. S2). There is only a relatively weak correlation between Fe_{HR}/Fe_T and CIA (chemical index of alteration, a proxy for continental weathering; Nesbitt and Young, 1982) (R^2 = 0.12, p = 0.01, Fig. 5) across the T-OAE CIE interval, and a similarly weak correlation occurs through the entire succession (R^2 = 0.13, p = 0.0015, Fig. 5). These data indicate that the observed Fe_{HR} enrichments were unlikely to have been derived primarily from enhanced chemical weathering and terrestrial input during the T-OAE CIE interval. Increased input of terrestrial organic matter during the T-OAE CIE interval has been demonstrated based on previously published TOC/N from the Sakuraguchi-dani section, coincident with a sediment-coarsening trend inferred from Rb/Zr data (Kemp and Izumi, 2014). However, negligible or weak correlations are observed between Fe_{HR}/Fe_T and TOC/N or Rb/Zr (Fig. 6). These data thus support our inference that enhanced chemical weathering or terrigenous flux across the T-OAE CIE interval at the Sakuraguchi-dani section had only a limited influence on the Fe_{HR} enrichments we observe.

The hydrography in the Panthalassa, partly responsible for controlling regional circulation and sites of upwelling (Parrish and Curtis, 1982), could have been altered due to a global sea level rise during the Toarcian (Hallam, 1981) – although coeval ocean circulation of Panthalassa, particularly at margins such as at the Sakuraguchi-dani section, is poorly understood. Currents distributed at mid-latitudes in the northern hemisphere may have flowed towards the Sakuraguchi-dani section, owing to prevailing winds from Panthalassa towards the eastern margin of Pangea in the late Early Jurassic (Parrish and Curtis, 1982; Scotese and Moore, 2014). Currents could then have flowed parallel with the coast after reaching the shore, undergoing Ekman transport and potentially promoting regional upwelling. Additionally, enhanced hydrological cycling at the Sakuraguchi-dani section, including evidence for storm activity and high-energy sediment transport (Izumi et al., 2018a), would have facilitated water-column mixing. Therefore, regional upwelling and water-column mixing on the Panthalassic margin around the Sakuraguchi-dani depositional site could have been promoted. Under these conditions, the strongly anoxic-ferruginous deep waters (saturated with dissolved Fe^{2+}) we document from the Sakahogi section could have been upwelled onto the shelf (Fig. 7). Oxidation of this Fe^{2+} in oxic shallow waters, and subsequent deposition largely *in situ*, would thus be responsible for the enhanced Fe_{HR}/Fe_T ratios (with Fe_{HR} being dominated by Fe (oxyhydr)oxides; Fig. 3A).

Although a potentially viable mechanism, the lack of paleo-productivity data or detailed information on regional paleoceanography at the Sakuraguchi-dani section makes it difficult to accurately assess any change in local/regional upwelling/productivity. In addition, seawater anoxia associated with intense upwelling tends to occur on the slope (i.e., relatively deeper waters) like the Peru Margin (e.g., Arthur et al., 1998), while much shallower waters on the shelf could be more susceptible to perturbations and remain relatively oxygenated (e.g., the manganese flux analysis of California Margin sediment indicating oxic waters on the shallow continental shelf; Johnson et al., 1992), similar to the scenario at the Sakuraguchi-dani section. Thus, local factors can significantly influence seawater redox conditions even in an area of upwelling.

Hydrothermal activity in the deep sea can also introduce reduced iron (Fe^{2+}) and Si-rich fluids, and this phenomenon could have affected our Sakahogi data. No visible mineralization in our analyzed samples was observed, however, and deposition of the bedded cherts at Inuyama was likely well away from the influence of any hydrothermal venting (Matsuda and Isozaki, 1991). The preservation of primary and globally representative geochemical signals such as osmium-isotope ratios (e.g., Kuroda et al., 2010) in the Inuyama area further suggests limited influence from hydrothermal fluids.

5.4 Redox conditions of Panthalassic deep waters during hyperthermal events in the Mesozoic

In addition to the T-OAE, other hyperthermal events occurred in the Mesozoic that were accompanied by marked global perturbations to the carbon cycle, severe environmental changes, and mass extinctions. These phenomena include the Permian–Triassic boundary event (PTB), the Triassic–Jurassic boundary event (TJB), and the early Aptian oceanic anoxic event (OAE1a, Early Cretaceous) (Korte et al, 2018; Hu et al., 2020). All of the above events were associated to a greater or lesser degree with the development of marine anoxia, which is often cited as playing a key role in driving ecosystem collapse (e.g. Meyer and Kump, 2008). Nevertheless, there exists significant spatiotemporal redox variability, especially in global open-ocean settings such as Panthalassa, which may obscure the redox control on bio-extinction.

The role and driving mechanisms of deep-ocean anoxia during these events is poorly studied. Pyrite framboid size analysis of Permian to Jurassic samples from the Mino-Tamba terrane of Japan indicates overall long-term (~80 Myr) oxygenation of Panthalassic deep waters, with three intervals (PTB, Spathian stage, and Toarcian stage) characterized by anoxic/euxinic conditions (Wignall, et al., 2010). The marine extinction at the PTB, the largest mass extinction of the Phanerozoic, has previously been attributed to widespread anoxia (Wignall and Twitchett, 1996). Sedimentological and geochemical evidence from Japan and British Columbia indicates an ~20 Myr suboxic to anoxic interval in Panthalassic deep waters, punctuated by water-column euxinia across the PTB (Isozaki, 1997). This low-oxygen state is consistent with a coeval expansion of seawater euxinia to the outer shelf associated with an active marine phosphorus cycle at the northern margin of Pangaea (Schobben et al., 2020). This study site (Festningen) connected the Boreal Sea and Panthalassa, suggesting development of seawater anoxia on a global scale (Schobben et al., 2020).

Across the TJB, high-resolution inorganic and organic geochemical proxies (Fe-speciation, redox-sensitive trace elements, and biomarkers) from Europe argue for expanded shallow-water anoxia, and even photic-zone euxinia, leading to the end-Triassic mass extinction (e.g., Fox et al., 2022; He et al., 2022). However, redox-sensitive elements and nitrogen isotopes from the Panthalassic pelagic section at Inuyama suggest more oxic conditions in Panthalassic deep waters across the TJB (Fujisaki et al., 2016). Redox conditions in the pelagic Pacific Ocean varied spatially during the OAE1a in the Cretaceous (e.g., Dumitrescu and Brassell, 2006; Bauer et al., 2022). Lower Cretaceous Pacific Ocean pelagic sediments at Site 1207 from the Shatsky Rise around the paleo-equator record organic matter-rich deposition at the onset of the OAE1a, and TOC/S ratios from this site likely reflect deep-water Fe-limited and euxinic conditions (Dumitrescu and Brassell, 2006). Such redox change around the paleo-equator may have resulted from enhanced productivity on the basis of biomarker analyses from Sites 1207 and 1213 in the west-central Pacific Ocean (Dumitrescu and Brassell, 2005), consistent with the common occurrence of organic-rich sediments within this area (e.g., Dean et al., 1981; Baudin and Sachsenhofer, 1996). However, redox-sensitive element and Fe-speciation data from DSDP Site 463 indicate persistent anoxic-ferruginous conditions in Pacific deep waters during OAE1a, associated with a significant drop of seawater sulfate concentration (Bauer et al., 2022).

Our analysis of the Panthalassic redox record suggests that a prolonged deep-water anoxic-ferruginous interval spanned the time interval from the late Pliensbachian to the onset of the T-OAE CIE interval, and at least local/regional Panthalassic deep-water euxinia occurred during the T-OAE CIE interval, in line with the findings of Kemp et al. (2022b). However, the scale of the biological response does not clearly map onto the occurrence of deep-ocean anoxia. For instance, both the T-OAE and PTB have evidence of deep-water anoxia but the scale of extinction is markedly different (see Hu et al., 2020 for a review). Indeed, the deep ocean apparently remained oxygenated across the TJB (Fujisaki et al., 2016), despite this event being one of the Phanerozoic ‘big five’ extinctions. The mechanisms that are able to drive the deep-ocean anoxia are also a matter of debate, since the relative contributions from a warming-driven slowing of circulation resulting in isolation and deoxygenation of the vast ocean interior, and the transport of sufficient nutrients across large distances from their weathering source to fuel enhanced productivity are difficult to evaluate. Nutrients seem to be key, but exactly how the open ocean comes to be nutrient rich is not yet well understood (see Winguth and Winguth, 2012; Meyer et al, 2008). Some of these questions may only be resolved by a better understanding of the spatial distribution of deep-sea anoxia, something that is only accessible via modelling approaches unless more deep-water sections are identified.

Conclusions

Our data indicate that the Panthalassic deep-water site of Sakahogi, characterized by radiolarian cherts, was predominantly anoxic-ferruginous from the late Pliensbachian to the onset of the T-OAE CIE interval. Enhanced sulfide production occurred in sediments around the Pl/To boundary (intercalated with possible oxic episodes), and the development of at least intermittently euxinic bottom waters occurred across the T-OAE CIE interval. Conditions became more oxygenated thereafter. On the Panthalassic margin at the Sakuraguchi-dani section, the ostensible evidence for pervasive anoxia indicated by Fe-speciation data is at odds with independent geochemical, sedimentological, and paleoecological evidence for predominantly oxygenated conditions. We suggest that the shallow-water environment received upwelled deep waters rich in Fe^{2+}, which was oxidized and deposited *in situ*, thus leading to the distinct Fe-speciation signature. The deep-water euxinia in the Panthalassa revealed by our analysis contrasts with evidence from the older Triassic–Jurassic boundary event, where deep ocean waters may have remained largely oxic.

Acknowledgements

This work was supported by the National Natural Science Foundation of China (Grant No. 41888101, 42272033, 42172039, and 42230208), and the National Recruitment Program for Young Professionals (P.R. China) to DBK. RJN, SWP and TH are supported by grant NE/N018559/1 from the Natural Environment Research

Council. This manuscript is a contribution to the Integrated Understanding of the Early Jurassic Earth System and Timescale (JET) ICDP project and IGCP 739.

Appendix A. Supplementary material

Supplementary material related to this article can be found on-line at https://

References

Alcott, L.J., Krause, A.J., Hammarlund, E.U., Bjerrum, C.J., Scholz, F., Xiong, Y., Hobson, A.J., Neve, L., Mills, B.J.W., März, C., Schnetger, B., Bekker, A., Poulton, S.W., 2020. Development of iron speciation reference materials for palaeoredox analysis. Geostand. Geoanal. Res. 44, 581–591.

Algeo, T.J., Tribovillard, N., 2009. Environmental analysis of paleoceanographic systems based on molybdenum–uranium covariation. Chemical Geology 268, 211–225.

Anderson, R.F., Fleisher, M.Q., LeHuray, A.P., 1989. Concentration, oxidation state, and particulate flux of uranium in the Black Sea. Geochimica et Cosmochimica Acta 53, 2215–2224.

Ando, A., Kodama, K., Kojima, S., 2001. Low-latitude and Southern Hemisphere origin of Anisian (Triassic) bedded chert in the Inuyama area, Mino terrene, Central Japan. J. Geophys. Res. 106, 1973–1986.

Arthur, M.A., Dean, W.E., Laarkamp, K., 1998. Organic carbon accumulation and preservation in surface sediments on the Peru margin. Chemical Geology 152, 273–286.

Baudin, F., Sachsenhofer, R.F., 1996. Organic geochemistry of Lower Cretaceous sediments from Northwestern Pacific guyots (ODP Leg 143). Organic Geochemistry 25, 311–324.

Bauer, K.W., Bottini, C., Katsev, S., Jellinek, M., Francois, R., Erba, E., Crowe, S.A., 2022. Ferruginous oceans during OAE1a and collapse of the marine sulfate pool. Earth and Planetary Science Letters 578, 117324.

Canfield, D.E., Raiswell, R., Westrich, J.T., Reaves, C.M., Berner, R.A., 1986. The use of chromium reduction in the analysis of reduced inorganic sulfur in sediments and shales. Chem. Geol. 54, 149–155.

Canfield, D.E., Raiswell, R., Bottrell, S.H., 1992. The reactivity of sedimentary iron minerals toward sulfide. American Journal of Science 292, 659–683.

Chen, W., Kemp, D.B., He, T., Huang, C., Jin, S., Xiong, Y., Newton, R.J., 2021. First record of the early Toarcian oceanic anoxic event in the Hebrides Basin (UK) and implications for redox and weathering changes. Global and Planetary Change 207, 103685.

Chen, W., Kemp, D.B., Newton, R.J., He, T., Huang, C., Cho, T., Izumi, K., 2022. Major sulfur cycle perturbations in the Panthalassic Ocean across the Pliensbachian-Toarcian boundary and the Toarcian Oceanic Anoxic Event. Global and Planetary Change 215, 103884.

Dean, W.E., Claypool, G.E., Thiede, J., 1981. Origin of organic–carbon-rich Mid-Cretaceous limestones, Mid-Pacific Mountains and Southern Hess Rise. In: Thiede, J., Vallier, T.L., et al., (Eds.), Initial Reports of the Deep Sea Drilling Project, vol. 62. U.S. Government Printing Office, Washington, DC, pp. 877–890.

Dickson, A.J., Gill, B.C., Ruhl, M., Jenkyns, H.C., Porcelli, D., Idiz, E., Lyons, T.W., van den Boorn, S.H., 2017. Molybdenum-isotope chemostratigraphy and paleoceanography of the Toarcian Oceanic Anoxic Event (Early Jurassic). Paleoceanography 32, 813–829.

Dumitrescu, M., Brassell, S.C., 2005. Biogeochemical assessment of sources of organic matter and paleoproductivity during the early Aptian Oceanic Anoxic Event at Shatsky Rise, ODP Leg 198. Organic Geochemistry 36, 1002–1022.

Dumitrescu, M., Brassell, S.C., 2006. Compositional and isotopic characteristics of organic matter for the early Aptian Oceanic Anoxic Event at Shatsky Rise, ODP Leg 198. Palaeogeography, Palaeoclimatology, Palaeoecology 235, 168–191.

Erba, E., Cavalheiro, L., Dickson, A.J., Faucher, G., Gambacorta, G., Jenkyns, H.C. and Wagner, T., 2022. Carbon- and oxygen-isotope signature of the Toarcian Oceanic Anoxic Event: insights from two Tethyan pelagic sequences (Gajum and Sogno Cores–Lombardy Basin, northern Italy). Newsletters on Stratigraphy 55, 451–477.

Erickson, B.E., Helz, G.R., 2000. Molybdenum (VI) speciation in sulfidic waters: stability and lability of thiomolybdates. Geochimica et Cosmochimica Acta 64, 1149–1158.

Fox, C.P., Whiteside, J.H., Olsen, P.E., Cui, X., Summons, R.E., Idiz, E., Grice, K., 2022. Two-pronged kill mechanism at the end-Triassic mass extinction. Geology 50, 448–453.

Fujisaki, W., Sawaki, Y., Yamamoto, S., Sato, T., Nishizawa, M., Windley, B.F., Maruyama, S., 2016. Tracking the redox history and nitrogen cycle in the pelagic Panthalassic deep ocean in the Middle Triassic to Early Jurassic: Insights from redox-sensitive elements and nitrogen isotopes. Palaeogeography, Palaeoclimatology, Palaeoecology 449, 397–420.

Gill, B.C., Lyons, T.W., Jenkyns, H.C., 2011. A global perturbation to the sulfur cycle during the Toarcian Oceanic Anoxic Event. Earth and Planetary Science Letters 312, 484–496.

Golonka J., 2007. Late Triassic and Early Jurassic palaeogeography of the world: Palaeogeography, Palaeoclimatology, Palaeoecology 244, 297–307.

Gröcke, D.R., Hori, R.S., Trabucho-Alexandre, J., Kemp, D.B., Schwark, L., 2011. An open ocean record of the Toarcian oceanic anoxic event. Solid Earth 2, 245–257.

Hallam, A., 1981. A revised sea-level curve for the early Jurassic. Journal of the Geological Society 138, 735–743.

He, T., Wignall, P.B., Newton, R.J., Atkinson, J.W., Keeling, J.F., Xiong, Y., Poulton, S.W., 2022. Extensive marine anoxia in the European epicontinental sea during the end-Triassic mass extinction. Global and Planetary Change 210, 103771.

Hesselbo, S.P., Grocke, D.R., Jenkyns, H.C., Bjerrum, C.J., Farrimond, P., Bell, H.S.M., Green, O.R., 2000. Massive dissociation of gas hydrate during a Jurassic oceanic anoxic event. Nature 406, 392–395.

Helz, G.R., Miller, C.V., Charnock, J.M., Mosselmans, J.F.W., Pattrick, R.A.D., Garner, C.D., Vaughan, D.J., 1996. Mechanism of molybdenum removal from the sea and its concentration in black shales: EXAFS evidence. Geochimica et Cosmochimica Acta 60, 3631–3642.

Hu, X., Li, J., Han, Z., Li, Y., 2020. Two types of hyperthermal events in the Mesozoic-Cenozoic: Environmental impacts, biotic effects, and driving mechanisms. Science China Earth Sciences 63(8), 1041–1058.

Ikeda, M., Hori, R.S., 2014. Effects of Karoo–Ferrar volcanism and astronomical cycles on the Toarcian oceanic anoxic events (Early Jurassic). Palaeogeography, Palaeoclimatology, Palaeoecology, 410, 134–142.

Ikeda, M., Hori, S.R., Ikehara, M., Miyashita, R., Chino, M., 2018. Carbon cycle dynamics linked with Karoo-Ferrar volcanism and astronomical cycles during Pliensbachian–Toarcian (Early Jurassic). Global and Planetary Change 170, 163–171.

Isozaki, Y., 1997. Permo-Triassic boundary superanoxia and stratified superocean: records from lost deep sea. Science 276(5310), 235–238.

Izumi, K., Miyaji, T., Tanabe, K., 2012. Early Toarcian (Early Jurassic) oceanic anoxic event recorded in the shelf deposits in the northwestern Panthalassa: evidence from the Nishinakayama Formation in the Toyora area, west Japan. Palaeogeography, Palaeoclimatology, Palaeoecology 315, 100–108.

Izumi, K., Kemp, D.B., Itamiya, S., Inui, M., 2018a. Sedimentary evidence for enhanced hydrological cycling in response to rapid carbon release during the early Toarcian oceanic anoxic event. Earth and Planetary Science Letters 481, 162–170.

Izumi, K., Endo, K., Kemp, D.B., Inui, M., 2018b. Oceanic redox conditions through the late Pliensbachian to early Toarcian on the northwestern Panthalassa margin: Insights from pyrite and geochemical data. Palaeogeography, Palaeoclimatology, Palaeoecology 493, 1–10.

Izumi, K., Suzuki, K., Kemp, D.B., Lizuka, T., 2020. Palaeogeographic and tectonic setting of the Lower Jurassic (Pliensbachian-Toarcian) Nishinakayama Formation, Toyora Group, SW Japan. Geological Journal 55, 862–874.

Jenkyns, H.C., 1988. The early Toarcian (Jurassic) anoxic event-stratigraphic, sedimentary, and geochemical evidence. American Journal of Science 288, 101–151.

Johnson, K.S., Berelson, W.M., Coale, K.H., Coley, T.L., Elrod, V.A., Fairey, W.R., IAMS, H.D., Kilgore, T.E., Nowicki, J.L., 1992. Manganese flux from continental margin sediments in a transect through the oxygen minimum. Science 257, 1242–1245.

Kemp, D.B., Izumi, K., 2014. Multiproxy geochemical analysis of a Panthalassic margin record of the early Toarcian oceanic anoxic event (Toyora area, Japan). Palaeogeography, Palaeoclimatology, Palaeoecology 414, 332–341.

Kemp, D.B., Baranyi, V., Izumi, K., Burgess, R.D., 2019. Organic matter variations and links to climate across the early Toarcian oceanic anoxic event (T-OAE) in Toyora area, southwest Japan. Palaeogeography, Palaeoclimatology, Palaeoecology 530, 90–102.

Kemp, D.B., Selby, D., Izumi, K., 2020. Direct coupling between carbon release and weathering during the Toarcian oceanic anoxic event. Geology 48, 976–980.

Kemp, D.B., Suan, G., Fantasia, A., Jin, S., Chen, W., 2022a. Global organic carbon burial during the Toarcian oceanic anoxic event: Patterns and controls. Earth-Science Reviews 231, 104086.

Kemp, D.B., Chen, W., Cho, T., Algeo, T.J., Shen, J., Ikeda, M., 2022b. Deep-ocean anoxia across the Pliensbachian–Toarcian boundary and the Toarcian Oceanic Anoxic Event in the Panthalassic Ocean. Global and Planetary Change 212, 103782.

Korte, C., Ruhl, M., Pálfy, J., Ullmann, C.V., and Hesselbo, S.P., 2018. Chemostratigraphy across the Triassic–Jurassic boundary. Chemostratigraphy Across Major Chronological Boundaries 183–210.

Kuroda, J., Hori, R.S., Suzuki, K., Gröcke, D.R., Ohkouchi, N., 2010. Marine osmium isotope record across the Triassic–Jurassic boundary from a Pacific pelagic site. Geology 38, 1095–1098.

Little, C.T., Benton, M.J., 1995. Early Jurassic mass extinction: a global long-term event. Geology 23, 495–498.

Littler, K., Hesselbo, S.P., Jenkyns, H.C., 2010. A carbon-isotope perturbation at the Pliensbachian–Toarcian boundary: evidence from the Lias Group, NE England. Geol. Mag. 147, 181–192.

Liu, J., Algeo, T.J., 2020. Beyond redox: Control of trace-metal enrichment in anoxic marine facies by watermass chemistry and sedimentation rate. Geochimica et Cosmochimica Acta 287, 296–317.

Lyons T.W., Severmann, S., 2006. A critical look at iron paleoredox proxies: New insights from modern euxinic marine basins. Geochimica et Cosmochimica Acta 70, 5698–5722.

Matsuda, T., Isozaki, Y., 1991. Well-documented travel history of Mesozoic pelagic chert in Japan: From remote ocean to subduction zone. Tectonics 10, 475–499.

McLennan, S.M., 1993. Weathering and global denudation. The Journal of Geology 101, 295–303.

McLennan, S.M., 2001. Relationships between the trace element composition of sedimentary rocks and upper continental crust. Geochemistry, Geophysics, Geosystems 2(4).

Meyer, K.M., Kump, L.R., 2008. Oceanic euxinia in Earth history: causes and consequences. Annual Review of Earth and Planetary Sciences 36(1), 251–288.

Meyer, K. M., Kump, L.R., Ridgwell, A., 2008. Biogeochemical controls on photic-zone euxinia during the end-Permian mass extinction. Geology 36(9), 747–750.

Nesbitt, H., Young, G.M., 1982. Early Proterozoic climates and plate motions inferred from major element chemistry of lutites. Nature 299(5885), 715–717.

Newton, R.J., Reeves, E.P., Kafousia, N., Wignall, P.B., Bottrell, S.H., Sha, J.-G., 2011. Low marine sulfate concentrations and the isolation of the European epicontinental sea during the Early Jurassic. Geology 39, 7–10.

Parrish, J.T., Curtis, R.L., 1982. Atmospheric circulation, upwelling, and organic-rich rocks in the Mesozoic and Cenozoic eras. Palaeogeography, Palaeoclimatology, Palaeoecology 40, 31–66.

Poulton, S.W., Raiswell, R., 2002. The low-temperature geochemical cycle of iron: from continental fluxes to marine sediment deposition. American Journal of Science 302, 774–805.

Poulton, S.W., Krom, M.D., Raiswell, R., 2004. A revised scheme for the reactivity of iron (oxyhydr) oxide minerals towards dissolved sulfide. Geochimica et cosmochimica acta 68, 3703–3715.

Poulton, S.W., Canfield, D.E., 2005. Development of a sequential extraction procedure for iron: implications for iron partitioning in continentally derived particulates. Chemical Geology 214, 209–221.

Poulton, S.W., Canfield, D.E., 2011. Ferruginous conditions: a dominant feature of the ocean through Earth's history. Elements 7, 107–112.

Poulton, S.W., 2021. The Iron Speciation Paleoredox Proxy. Cambridge University Press, Geochemical Tracers in Earth System Science.

Raiswell, R., Canfield, D.E., 1998. Sources of iron for pyrite formation in marine sediments. American Journal of Science 298, 219–245.

Remírez, M., Algeo, T.J., 2020. Carbon-cycle changes during the Toarcian (Early Jurassic) and implications for regional versus global drivers of the Toarcian oceanic anoxic event. Earth-Science Reviews 209, 103283.

Schobben, M., Foster, W.J., Sleveland, A., Zuchuat, V., Svensen, H.H., Planke, S., Bond, D.P.G., Marcelis, F., Newton, R.J., Wignall, P.B., Poulton, S.W., 2020. A nutrient control on marine anoxia during the end-Permian mass extinction. Nature Geoscience 13(9), 640–646.

Scotese, C.R., 2001. Atlas of Earth History 1, Paleogeography. Arlington, Texas: PALEOMAP Project.

Scotese, C.R., Moore, T., 2014. Atlas of Phanerozoic Upwelling Zones (Mollweide Projection), Volumes 1–6, PALEOMAP Project PaleoAtlas for ArcGIS, PALEOMAP Project, Evanston, IL. https://doi.org/10.13140/2.1.2545.3125.

Them, T.R., Gill, B.C., Caruthers, A.H., Gerhardt, A.M., Gröcke, D.R., Lyons, T.W., Marroquín, S.M., Nielsen, S.G., Trabucho Alexandre, J.P., Owens, J.D., 2018. Thallium isotopes reveal protracted anoxia during the Toarcian (Early Jurassic) associated with volcanism, carbon burial, and mass extinction. Proceedings of the National Academy of Sciences 115, 6596–6601.

Wei, G., Chen, T., Poulton, S.W., Lin, Y., He, T., Shi, X., Chen, J., Li, H., Qiao, S., Liu, J., Li, D., Ling, H., 2021. A chemical weathering control on the delivery of particulate iron to the continental shelf. Geochimica et Cosmochimica Acta 308, 204–216.

Wignall, P.B., Twitchett, R.J., 1996. Oceanic anoxia and the end Permian mass extinction. Science 272(5265), 1155–1158.

Wignall, P.B., Bond, D.P., Kuwahara, K., Kakuwa, Y., Newton, R.J., Poulton, S.W., 2010. An 80 million year oceanic redox history from Permian to Jurassic pelagic sediments of the Mino-Tamba terrane, SW Japan, and the origin of four mass extinctions. Global and Planetary Change 71, 109–123.

Winguth, C., Winguth, A.M., 2012. Simulating Permian–Triassic oceanic anoxia distribution: Implications for species extinction and recovery. Geology 40, 127–130.

Figures

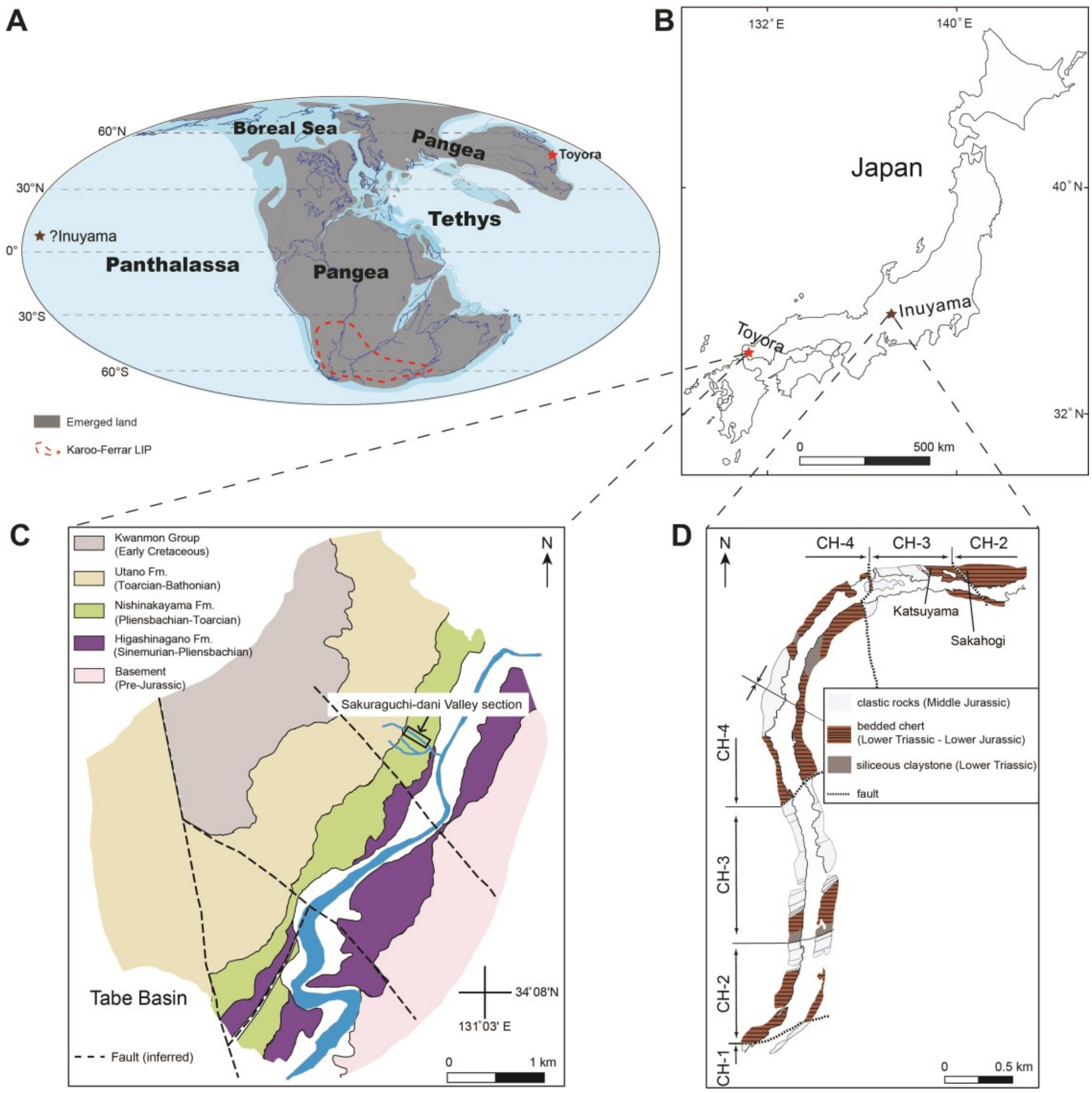

Fig. 1. (A) Paleogeographic map showing the locations of the Toyora (red star, Sakuraguchi-dani section) and Inuyama (brown star, Sakahogi section) sites in the Jurassic. Modified from Golonka (2007) and Scotese (2001). (B) Map of Japan showing the modern locations of the Toyora (red star) and Inuyama (brown star) field areas. (C) Geological map showing the Sakuraguchi-dani section in the Tabe Basin, Toyora area. Redrawn from Kemp and Izumi (2014). (D) Geological map showing the Sakahogi section and Katsuyama section of the Inuyama area. Redrawn from Ikeda et al. (2018).

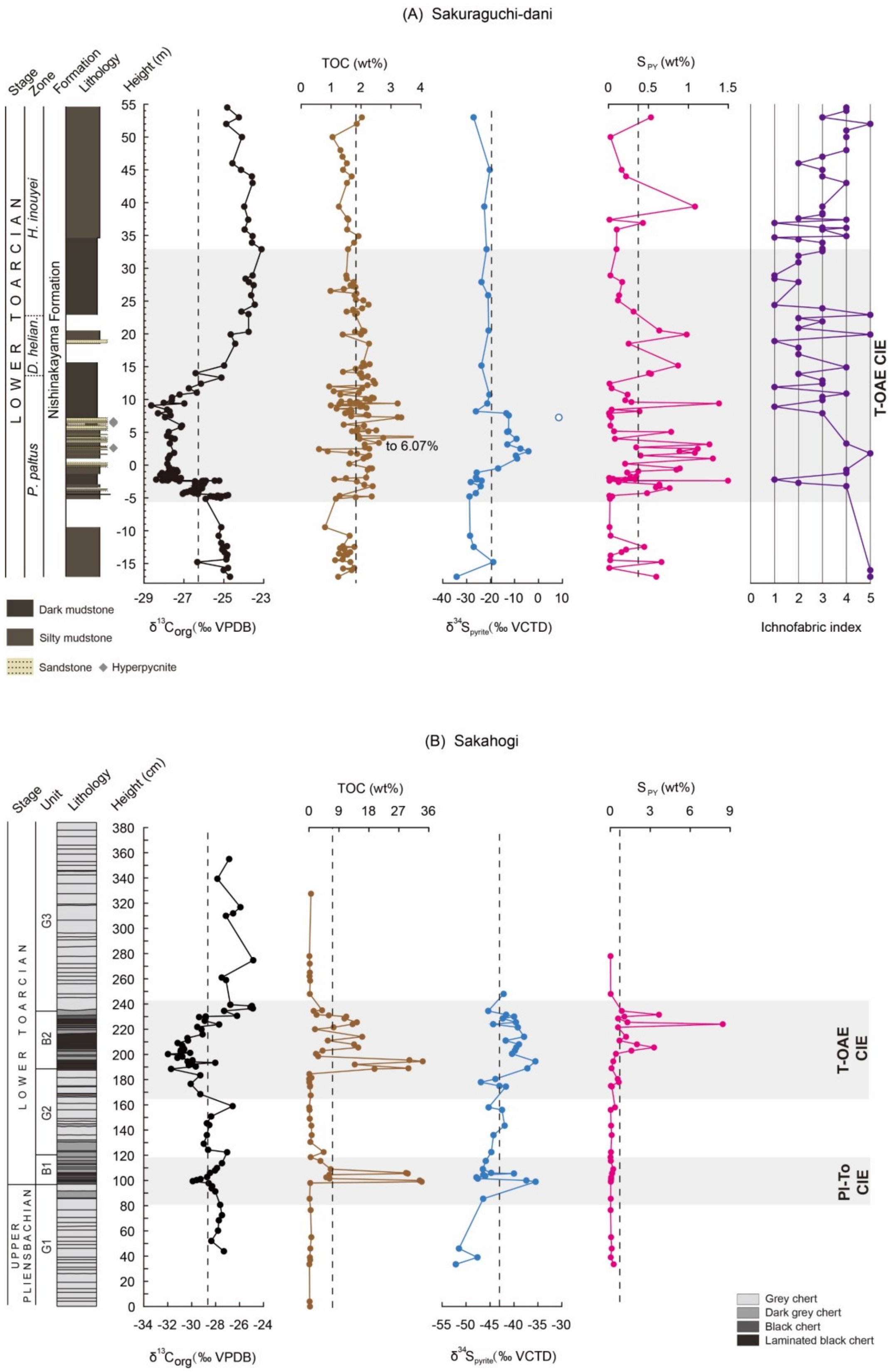

Fig. 2. Stratigraphy, organic-carbon isotopes ($\delta^{13}C_{org}$), total organic carbon (TOC), pyrite sulfur isotopes ($\delta^{34}S_{pyrite}$), pyrite sulfur concentrations (S_{PY}), and ichnofabric

index data from Sakuraguchi-dani (A) and Sakahogi (B) sections. $\delta^{13}C_{org}$, TOC and litho-/biostratigraphy at the Sakuraguchi-dani section are taken from Kemp and Izumi (2014) and Izumi et al. (2018a). Ichnofabric index data are from Izumi et al. (2012): 1 = no bioturbation, well laminated, 2 = weak bioturbation, laminated, 3 = bioturbated, poorly laminated, 4 = bioturbated, few laminations, 5 = well bioturbated, not laminated. $\delta^{13}C_{org}$ and lithostratigraphic units at the Sakahogi section are from Ikeda et al. (2018) and references therein. Lithostratigraphy and TOC data at the Sakahogi section are from Kemp et al. (2022b). $\delta^{34}S_{pyrite}$ and S_{PY} data from both sections are from Chen et al. (2022). Note that the unfilled blue circle in the Sakuraguchi-dani pyrite sulfur isotope profile represents the outlying value (see Chen et al., 2022 for details). The vertical dashed line represents the average value of each proxy at these sections. The T-OAE interval at the Sakuraguchi-dani section, and the Pl/To and T-OAE intervals at the Sakahogi section (shaded areas) are defined based on the carbon-isotope excursions (CIE) recorded at these sections.

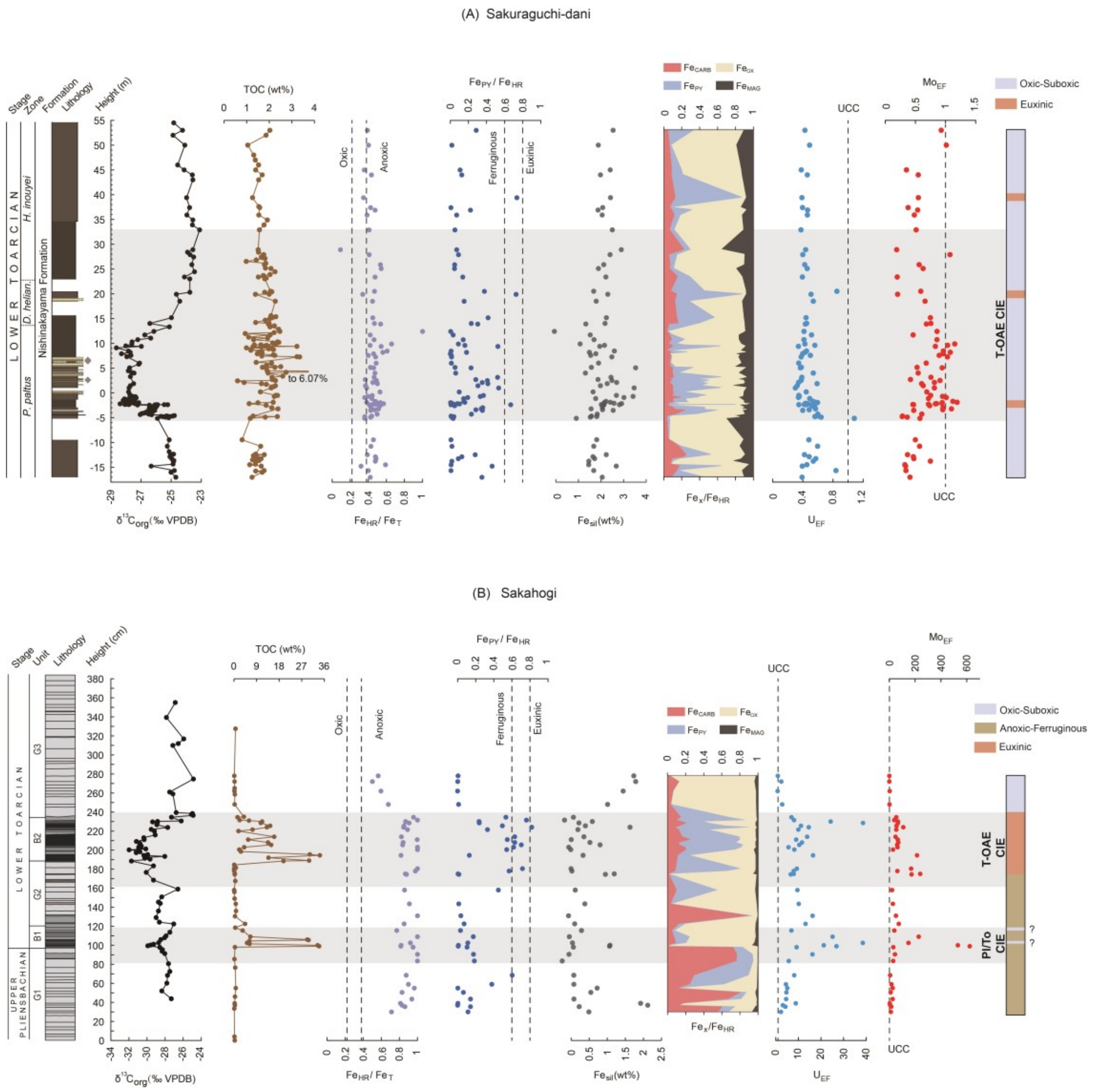

Fig. 3. Stratigraphy, $\delta^{13}C_{org}$, Fe-speciation, and redox-sensitive trace element data from the Sakuraguchi-dani (A) and Sakahogi (B) sections. Note that the colored bar on the far right of the figure indicates water-column redox conditions. Mo and U data at the Sakahogi section are from Kemp et al. (2022b).

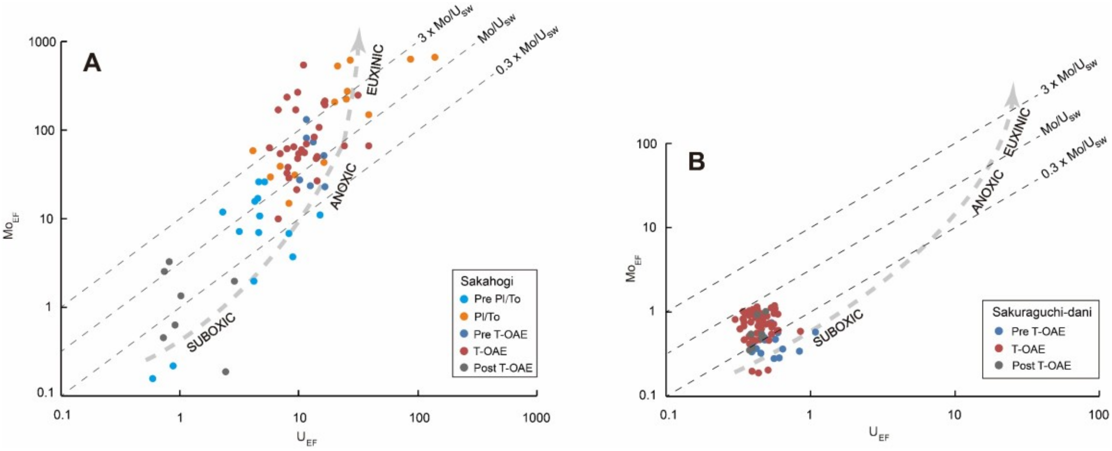

Fig. 4. Cross-plots of Mo_{EF} and U_{EF} data from the Sakahogi section (A) and the Sakuraguchi-dani section (B). Enrichment factors (EFs) herein are defined on the basis of average upper continental crust composition from McLennan (2001). See main text for details. Sakahogi data are from Kemp et al. (2022b). Cross-plots show the expected trends in Mo_{EF} versus U_{EF} for different redox scenarios. The dashed lines represent multiples (0.3, 1, and 3) of the Mo/U ratio of present-day seawater. See Algeo and Tribovillard (2009) for more details.

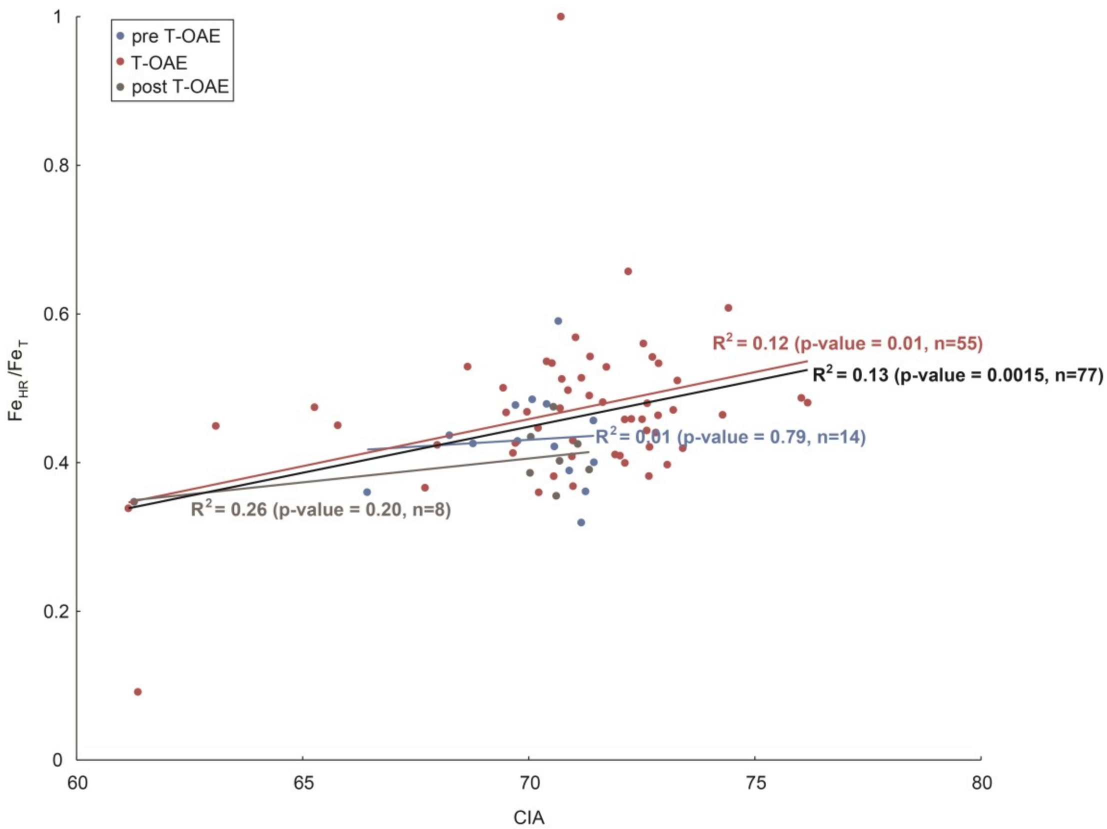

Fig. 5. Cross-plot of CIA (chemical index of alteration) versus Fe_{HR}/Fe_T through the Sakuraguchi-dani succession. The R^2 values represent the coefficient of determination for the correlations and p-values are the probability that an R^2 value at least as high would arise by chance. The black trend line, R^2 value, and p-value highlight the correlation for the entire succession. See Fig. S1 for the stratigraphic variation of CIA values at the Sakuraguchi-dani section.

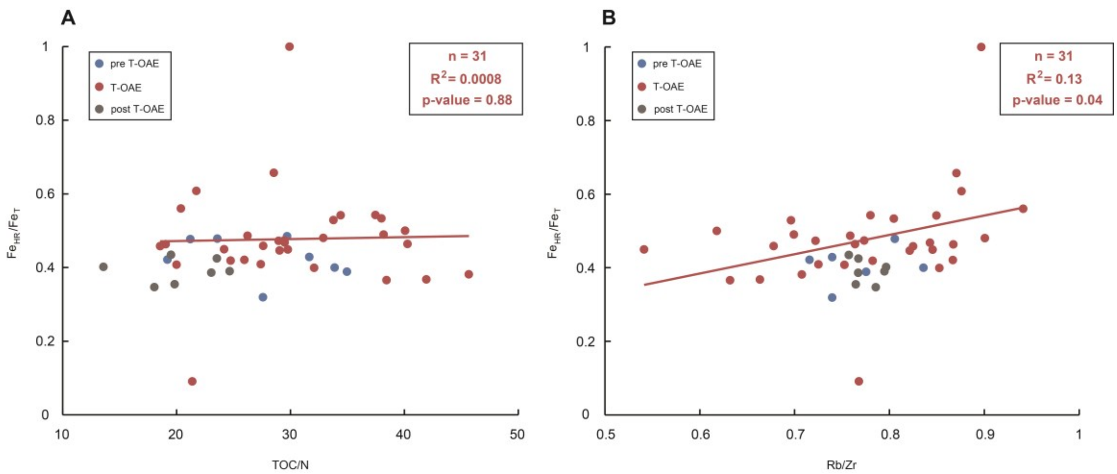

Fig. 6. Cross-plots of TOC/N versus Fe_{HR}/Fe_T (A) and Rb/Zr versus Fe_{HR}/Fe_T (B) through the Sakuraguchi-dani succession. The R^2 values represent the coefficient of determination for the correlations across the T-OAE CIE interval, and p-values are the probability that an R^2 value at least as high would arise by chance. TOC/N and Rb/Zr data are from Kemp and Izumi (2014), and stratigraphic variations of these data are shown in Fig. S1.

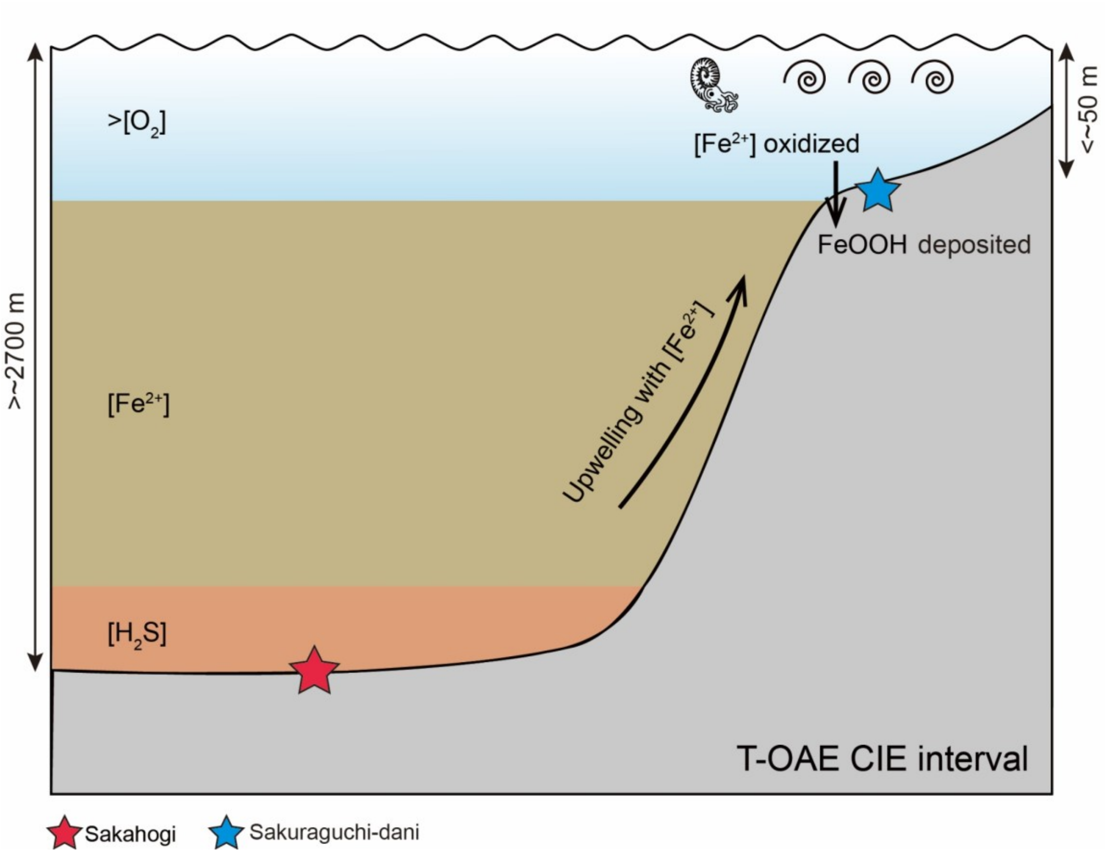

Fig. 7. Conceptual model of the Panthalassic Ocean chemistry during the T-OAE CIE interval. Deep-water euxinia occurred concurrent with oxic–suboxic conditions on the shelf and presumably anoxic-ferruginous intermediate waters. Upwelling could have brought deeper anoxic waters saturated with Fe^{2+} to the shelf area as a consequence of transgression and prevailing wind activity. The spiral lines denote frequent storm activity. See main text for further details.